IEEE Photonics Journal
An IEEE Photonics Society Publication

Open Access

4-D Imaging of Beating Tissues Using Optical Coherence Tomography

Volume 13, Number 3, June 2021

Guangju Zhang
Wei Wei

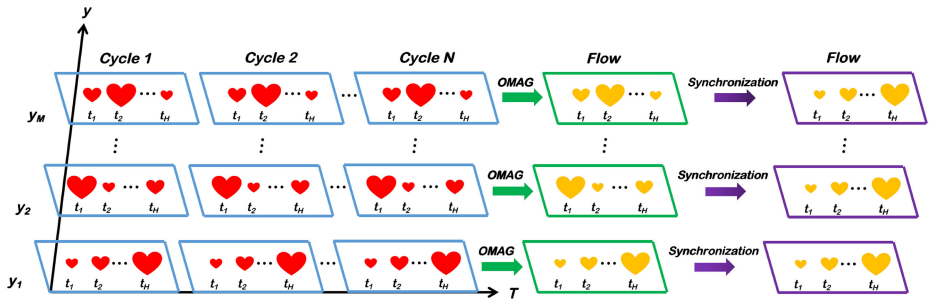

Illustration of T-OMAG approach for flow information in beating tissues

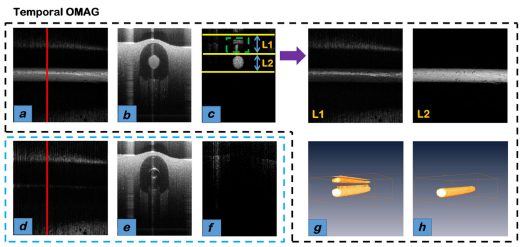

Plow imaging of beating the phantom

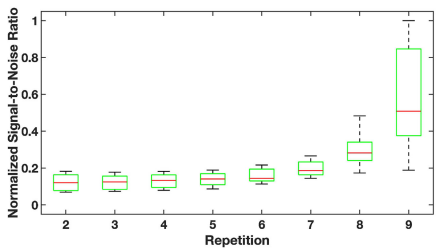

Normalized signal-to-noise ratio

DOI: 10.1109/JPHOT.2021.3076145

IEEE photonics SOCIETY

IEEE

4-D Imaging of Beating Tissues Using Optical Coherence Tomography

Guangju Zhang and Wei Wei

Department of Bioengineering, School of Engineering, University of Washington, Seattle, WA 98195 USA

DOI:10.1109/JPHOT.2021.3076145

Manuscript received February 22, 2021; revised April 22, 2021; accepted April 23, 2021. Date of publication April 27, 2021; date of current version May 17, 2021. This work was supported by National Heart, Lung and Blood Institute under Grant R01HL093140. Corresponding author: Guangju Zhang (e-mail: gjzhang7@uw.edu.)

Abstract: An imaging technique which reconstructs structure and flow in tissue with repetitive motion was developed using Optical Coherence Tomography (OCT). The demonstrated technique is able to accurately image both host tissue and flow at different time points during a cyclic motion, such as a cardiac cycle. Using tissue-mimicking phantoms, a phase-sensitive spectral-domain OCT system was combined with a cyclic-motion simulator to demonstrate the feasibility of the method. 3-D flow information at different time points in the cyclical motion was reconstructed in the temporal domain thus generating the 4-D imaging of the target tissue. This method could expand OCT-based studies such as those with cyclic motions in tissues, and open the door to 4-D vascular imaging of periodically moving tissues such as beating heart using OCT techniques.

Index Terms: Optical Coherence Tomography, instrumentation, 4-D imaging, beating tissues.

1. Introduction

Optical coherence tomography (OCT) is of great importance in both scientific and clinical research. Compared to other imaging technologies such as confocal microscopy [1], high-frequency ultrasonic imaging [2] and magnetic resonance imaging [3], OCT benefits from relatively higher resolution, faster acquisition time [4], [5]. To-date, OCT has been applied in the fields of ophthalmology [6], stomatology [7], dermatology [8], cardiovascular [9], gastroenterology [10], urology [11], etc.

In cardiovascular research, in addition to the clinical application in intravascular imaging, OCT is also applied in cardiac imaging of animal models such as mouse and chick. Researches in this field could help scientists in the study of cardiac diseases which are leading causes of deaths in United States [12]. Every year, about 25% of total deaths are caused by cardiac diseases while about 63% of cardiac deaths belong to ischemic cases [13]. Considering the above advantages, OCT techniques could greatly benefit research on ischemic cardiac diseases. For example, higher-resolution images of cardiac tissues and flow maps may be useful in comparing health hearts and infarcted hearts, generating a better understanding in pathological processes specially the infarcted coronary vasculatures and microvasculatures. In [14] and [15], the depth-resolved and 3-D flow map of coronary microvasculature was imaged in an *ex vivo* perfused rat heart using OCT. However, this report focused on a fixed sample which limited its application because a living heart beats cyclically with the contraction and expansion of myocardium to support blood circulation in the

body. Therefore, the flow map imaged from a beating heart will improve the research on perfusion dynamics of coronary vasculatures which is meaningful in studying heart diseases.

Similar to reconstructing flow dynamics in retinal [16]–[18] and mouse brain [19] vasculatures, imaging hearts with cyclical motions is especially challenging for OCT -based techniques because of motion-caused artifacts decreasing image quality. In [20], Kang et al. developed an accurate and fully automated algorithm to suppress the in-plane motion artifacts in OCT esophageal imaging. Also adopting a denoising algorithm, Gargesha et al. reported their OCT images of the quail embryonic heart, and the additive and speckle noise caused by biological motions could be reduced effectively from original images [21]. To image a chick embryonic heart, Mariampillai et al. used a retrospective-gated OCT and obtained the biological Doppler data to synchronize B-mode image sequences thus reconstructing the OCT imaging of the target tissue [22]. Liebling et al also developed retrospective-gated method combining an image reconstruction and applied this method in the 4-D imaging of zebra fish heart [23], [24]. Using an alternative non-gated 4-D imaging strategy combined with a simple and efficient postacquisition synchronization procedure that was presented in [25], Liu et al previously reported the reconstructed 4-D images indicating temporal blood flow dynamics of the chick embryonic heart [26]. In [27], Jenkins et al. reported a gated technique and obtained the 4-D embryonic cardiography using OCT. This technique would require the system to repeat B-scans at each lateral location of the beating tissue thus each B-frame would relate to a certain motion phase in cardiac cycles. Through the synchronization of the obtained data, B-frames of the same phase at all lateral locations of the tissue could be assembled to generate 3-D imaging and the 4-D movie recording a whole cardiac cycle could be obtained by bringing together all 3-D images. However, the imaging results in the report only contained structure images and no clear flow maps were given as imaging the perfusion would be more difficult. In [28], Grishina et al. adopted the method combing both speckle variance OCT (SV-OCT) and 4-D reconstruction technique, and achieved the 4-D blood flow and its Doppler imaging in the beating mouse embryonic heart thus recording the cyclic variation of blood flow in the heart. As the images were reconstructed by intensity signal, motion artifacts were avoided resulting in the high image quality. However, only large vasculatures were imaged with blood flow mapped while microvasculatures were not clearly obtained because of the residual structure information in images, which limited the further application of this method in hemodynamics study containing both coronary vasculatures and microvasculatures.

Optical microangiography (OMAG) is an effective method to image blood flow using OCT [29]. This method typically requires the system to repeat B-scans at the same transverse location of the tissue, and simple subtractions between these B-frames can extract the flow information at this location. Unfortunately, classic OMAG requires that B-frames have high correlation in static tissue regions. When there are cyclical motions in the target tissue, large motion amplitudes could decorrelate B-frames leading to the failure of the reduction of static information and flow information extraction. To-date, to the best of our knowledge, no report has been published on OMAG imaging of tissues like hearts with cyclical motions. Some techniques such as the perfusate applied in [30] could accurately simulate the perfusion dynamics in cardiac vascular networks in a beating heart, and the combination between the perfusate and OCT can be highly interesting and helpful, while obtaining OCT images of high quality at beating status is still the main challenge.

In this paper, an extended numerical method was developed to process the dynamic and static scatterers in cyclically beating tissues such as hearts. This method, Temporal OMAG (T-OMAG), records data of every transverse location over multiple repeat cycles. By collecting B-frames of the same motion phase from repeat cycles, OMAG calculation was enabled using these data and the flow information can be extracted at the corresponding location. To demonstrate the feasibility of this method, phantom tests were made using a Spectral-Domain OCT (SD-OCT) system that was combined with cardiac beating simulator. Two phantoms were applied that served as the displacement of the beating tissue in a heart. One phantom contained the larger tube acting as the coronary vasculature while the other phantom contained a smaller tube that served as the microvasculature. Clear images of the phantoms as well as the flow imaging in the tubes were reconstructed when the phantom was cyclically beating with the beat rate of 6 Hz which was set

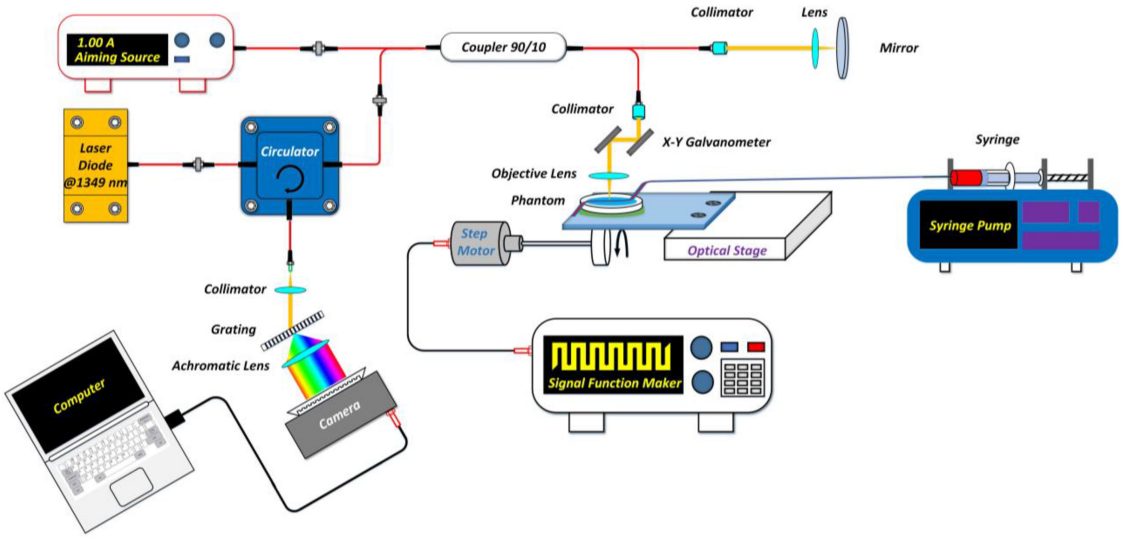

Fig. 1. Setup of the OCT system and motion simulator.

according to the living rat heart [31]. By bringing together all flow images at different time points, 4-D imaging of the flow map in tubes were generated indicating the perfusion dynamics of a whole cardiac cycle. These provided the high possibility for this method in the OCT imaging of both structure and flow map in cyclically beating heart.

2. Materials and Methods

2.1 Experimental System

Fig. 1 shows the experimental system. The spectral-domain Optical Coherence Tomography (SD-OCT) system was based on a fiber-based Michelson interferometer design. A superluminescent diode (SLD) that was centered at 1349 nm with the spectral bandwidth of 110 nm (LS2000B, Thorlabs Inc.), served as the laser source in the system and provided an axial resolution measured to be $\sim$7 μm in air. The laser was coupled into a circulator and split into two arms with a 90:10 and 2 $\times$ 2 coupler. In the reference arm, the laser was focused onto the reference mirror by a lens and then reflected into the coupler. In the sample arm, the laser passed through the 10 $\times$ objective lens (LSM02, Thorlabs Inc.) and was focused into the target tissue while the back-scattered light was recombined into the coupler. Thanks to the circulator, the recombined light from the two arms was routed to a high-speed spectrometer consisting of a 30-mm focal-length collimator, a transmitting grating with 1200 lines/mm, an achromatic lens with the focal length of 100 mm, and a 14-bit, 1024 pixels InGaAs line scan camera (SUI, Goodrich Corp.). The line scan rate of the camera reached up to $\sim$92 kHz while the spectrometer had a calculated spectral resolution of 0.141 nm generating the detectable depth range of $\sim$3.0 mm. The incident light power at the sample was $\sim$5 mW, resulting in a system sensitivity at the focus ($\sim$500 μm below the zero delay) measured at 105 dB. There were two galvo-scanners (6200H, Novanta/Cambridge Technology) to raster-scan the beam across the target tissue. One scanner corresponded to the x-axis and another is for y-axis direction. With the help of these two scanners, 3-D imaging of the target tissue can be obtained from the OCT system. To locate the imaging position, a 633-nm laser was used as the aiming source.

To simulate the cyclic motion of biological tissues, a step motor (17HD40005H-22B, Zyltech Inc.) which operated independently from OCT was used. A circular vibrator was fixed off-center to the rotor of the step motor. The target tissue was fixed to a rectangular plate where one end was fixed to the optical stage and the other end set against the vibrator. As the step motor rotated, the rotating vibrator would drive the target tissue to repeatedly move with the motion amplitude as much as

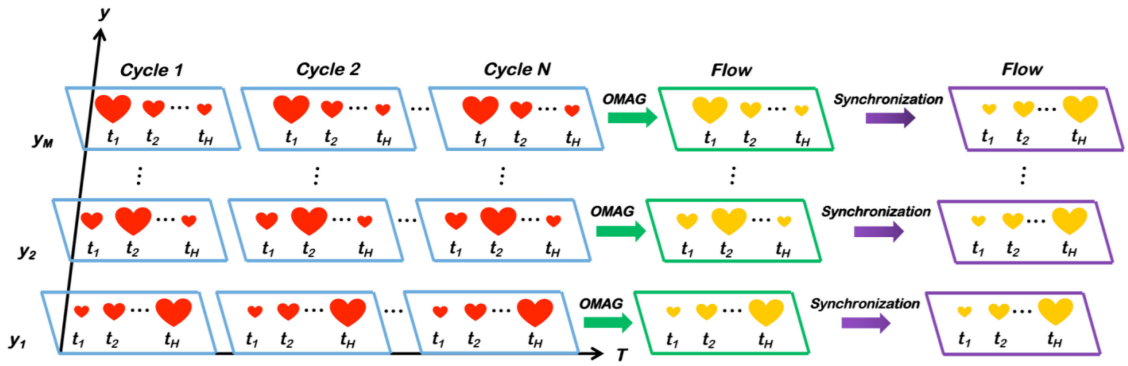

Fig. 2. Illustration of T-OMAG approach for flow information in beating tissues.

~0.4 mm. The rotation of the motor was driven by a function waveform generator (33220A, Agilent Inc.) which outputed a pulsed signal that periodically repeated at a rate of 1200 Hz, causing the target tissue to repeatably 'beat' with the rate of 6 Hz. Both the motion amplitude and the repetition rate were set according to the living rat heart [31].

The two phantoms applied in the experiment used a tubing of 0.5mm diameter and 0.22mm diameter to mimick coronary vasculature and microvasculature, respectively [14]. The background tissue was made with agar and gelatin [32]. 7-g gelatin and 120-mg agar were first mixed with 150-ml distilled water and then stirred with a heating plate until the powders were completely dissolved. The tubing was located close to the mixture surface thus being fixed till the mixture solidified. 10% intralipid was injected into the tubing from a syringe that was driven by a step-pumper (Fusion 100, Chemyx Inc.). The liquid flow speed was maintained at 0.1 and 0.5 mm/s in the large and small tubes respectively.

2.2 Temporal OMAG

Assuming a target tissue is moving with a certain low-frequency, a motion cycle can be divided into a set number of time points which correspond to the beating motion phases. In Fig. 2, motion phases are represented by red hearts of different sizes while the corresponding time reference of each motion phase is represented by t_1, t_2, … t_H (T-axis). The y-axis corresponds to the transverse direction of the target tissue, which is divided into different spatial points of y_1, y_2, … y_M. Repeated B-scans are acquired at every transverse location and there should be a fixed time offset between two B-frames at this spatial point such as y_1. This allows for B-frames to precisely correspond to a fixed temporal point in the cyclic motion of the tissue. A B-frame during one motion cycle can be paired with a B-frame in the next motion cycle if the frame rate is precisely designed according to beat rate and the number of time points in a motion cycle. This process will last for several motion cycles, thus the number of B-frames at one location will be determined by both cycle number and the number of time points in each motion cycle. For example, the number of B-frames at one location equals $N \times H$ while N is the number of motion cycles to be recorded at this location and H is the number of time points in a cycle. The B-frame rate should be $R \times H$ where R is the beat rate of the tissue. Assuming a high correlation of both the motion phase and scanned sample region during different motion cycles, the set of B-frames captured at each motion phase can be extracted from different cycles, and OMAG process can be achieved only by the data at the same motion phase in N cycles, while the flow information (orange heart in Fig. 1), will be separated from the static background. The equation describing the T-OMAG algorithm is given by:

$$Flow(x, y_s, z, t_l)\frac{1}{N-1}\sum_{i=0}^{N-1}\left|C_{i+1}\ (x, y_s, z, t_l) - C_i(x, y_s, z, t_l)\right|(S = 1, 2 \ldots M, l = 1, 2 \ldots H) \quad (1)$$

where *Flow* is the flow information, C_i is the complex OCT-signal, x, y_s and z represent positions in the lateral and depth directions respectively. y_s is the *s-th* of M locations while t_l is the *l-th* of H time

TABLE 1
Protocols Applied in Temporal OMAG and Classic OMAG

	Temporal OMAG	Classic OMAG
A-line Number	400	400
A-line Rate	67200 lps	67200 lps
B-frame Rate	126 fps	126 fps
B-scan Repetition	189	9
B-frame Number	75600	3600
Time Points	21	
Field of View	~2.5×2.5 mm^2	~2.5×2.5 mm^2
Scanning Time	~ 10 min	~ 57.14 s
Data Size	~ 57.6 GB	~ 2.44 GB

points. 4-D flow information of the whole target tissue will be obtained after the same operation is done from y_1 to y_M.

Considering the time offset generated by the moving y-axis scanner, there should be phase mismatching between two locations along y-axis. This is also shown in Fig. 2 where the recorded motion phases at y_1 to y_M are not completely consistent after OMAG process. This can be solved by the synchronizing approach that was reported before [23], [25], [28], [33]. After the OMAG process, the obtained 21 flow B-frames at y_1 were taken as the reference. Correlations between flow B-frames at y_1 and other locations should be achieved while the highest correlations always existed between flow B-frames relating to the same motion phase. The time mismatching can be corrected by bringing the same-phase frames into one volume. As shown in Fig. 2, the obtained flow B-frames by T-OMAG has already been temporally split facilitating the synchronization.

2.3 Scanning Protocols

The sensitivity of the T-OMAG algorithm is closely related to the scanning protocol of the system. A beating cycle was devided into 21 time points. Considering the 6-Hz motion rate of the target tissue, the B-frame rate was 126 frames per second (fps). Each B-frame contained 400 A-lines, and by setting the A-line rate of the camera to be 67200 lines per second (lps), a B-scan took ~6 ms with a time offset of ~2 ms (determined by the OCT system making B-frames precisely correspond to the time points in each cycle). The repetition number of B-frame at each transverse location in y-axis should be 189 when the motion cycle number was set to be 9. After finishing the B-scans at one location in y-axis, the galvo-scanner would move to the next location and repeat this process. As the 400 uniformly distributed locations in the y-axis were chosen, the whole data set consisted of 75600 B-frames, the total scanning time was 10 minutes with the size of ~57.6 GB. Each 3-D dataset covered a 2.5 $\times$ 2.5 mm^2 region.

As a reference, a protocol based on the classic OMAG was designed for the same sample and same scanned region as in T-OMAG. The B-scan in classic OMAG would have the same A-line number, 400 locations in y-axis, frame rate and A-line rate as the T-OMAG, while it is repeated 9 times at each y-axis location. That could generate 3600 B-frames in one 3-D dataset having the scanning time of ~57.14 s and ~2.44-GB size. Detailed protocols of both T-OMAG and classic OMAG are given in Table 1.

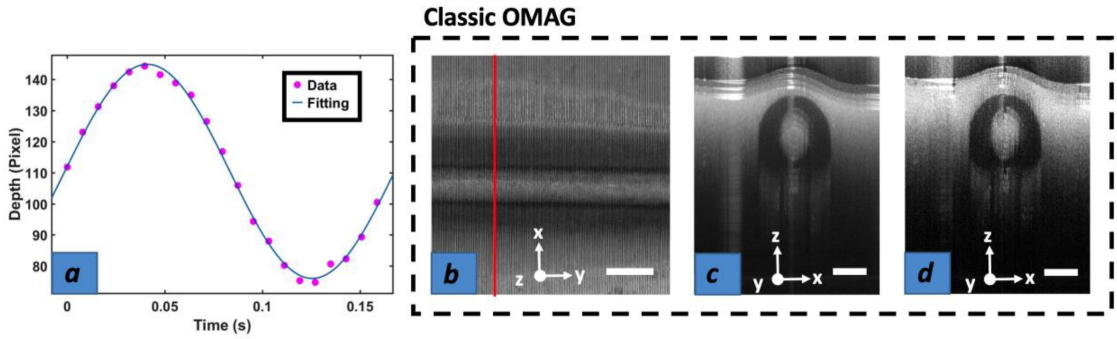

Fig. 3. a) Moving path of the large-tube phantom in depth direction. b) *En-face* maximum intensity projection (MIP) of the full-depth classic OMAG flow acquired in the large-tube phantom. c) and d) are showing cross sections of OCT structure and classic OMAG flow in the red line position in b) respectively. All scale bars in the figure represent 500 μm.

2.4 Data Analysis

The codes of classic OMAG, Temporal OMAG and the synchronization process were written in Matlab (Mathworks, MA, USA) to process OCT signals and produce optical images. Image segmentation was achieved by an in-house software written in Python [34]–[36].

3. Results

By tracking the movement of a fixed point on cross-section images of the large-tube phantom, the sample moving path was obtained. As shown in Fig. 3(a), in a motion cycle, the temporal trajectory of the phantom was approximate to a sine function. The maximum amplitude of the movement was calculated to be 70 pixels, corresponding to about 0.4 mm in the depth direction. With this large movement, the full-depth and *En-face* flow distribution obtained using classic OMAG is shown in Fig. 3(b), and the corresponding cross sections of OCT structure and classic-OMAG flow are shown in Fig. 3(c) and (d) respectively. In the three images, due to the decorrelation between different B-frames at the same transverse location, artifacts are easily observed in the cross sections of structure and flow pictures, and static backgrounds in the pictures make OCT structure and flow almost indistinguishable. It should be noted, vertical lines in Fig. 3(b) resulted from the decorrelation in static regions between different transverse locations, which was also caused by the motion of the phantom. In this demonstration, classic OMAG failed to reduce the impacts of the phantom motion in both artifacts and eliminating static background.

Using the same large-tube phantom, the T-OMAG flow information at one phase point in the total cycle is shown in Fig. 4. Fig. 4(a) is the *En-face* projection of the flow in the tubing while Fig. 4(b) and Fig. 4(c) show the corresponding cross sections of OCT structure and flow respectively. Obviously, T-OMAG can generate very clear imaging of the flow map in phantom. Due to accurately distributing B-frames at corresponding motion phases, at a certain transverse location, T-OMAG can effectively reduce the decorrelation of static region caused by motions, resulting in better performance than classic-OMAG to reduce artifact and extract flow information. Meanwhile, compared with Fig. 3(b), no obvious vertical lines exist in Fig. 4(a) indicating T-OMAG also possesses a much better correlation in flow information between different transverse locations. It should be noted, in Fig. 4(c), the noise in the green-dashed line was caused by the high scattering of the liquid perfusing in the tubing. This can be demonstrated by Fig. 4(d), (e) and (f) obtained with T-OMAG while there was no perfusion in the tubing, and the cross section of T-OMAG flow is almost dark but some noises caused by the high reflection indicating the absence of high-scattering. Applying the semi-automatic segmentation software, the layers of both tubing wall (L1) and core (L2), indicated by yellow lines in Fig. 4(c), can be separated which are shown to the right. By removing the layer of wall, the contrast in L2 was improved compared to the original image in Fig. 4(a). This also

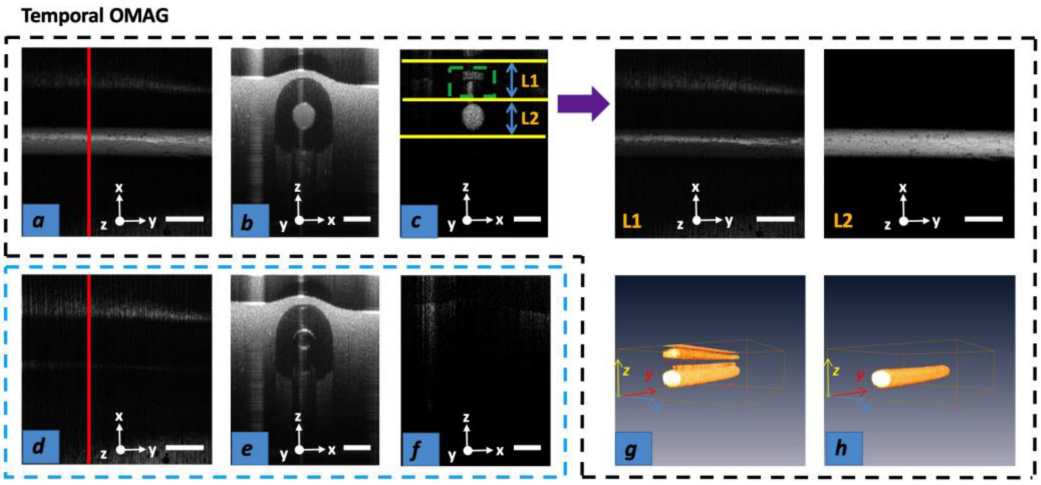

Fig. 4. a) *En-face* MIP of the full-depth T-OMAG flow image acquired in the large-tube phantom. b) Cross section of OCT structure in the red line position in a). c) Cross section of T-OMAG flow in the red line position in a) with segmentation layers of tubing wall (L1) and core (L2). The *en-face* images of L1 and L2 are shown to the right. d) *En-face* MIP of the full-depth T-OMAG flow image acquired in the phantom when no perfusion existed in the tubing. e) and f) are showing cross sections of OCT structure and T-OMAG flow in the red line position in d) respectively. g) and h) are 3-D flow distribution in the phantom before and after segmentation respectively. All scale bars in the figure represent 500 μm.

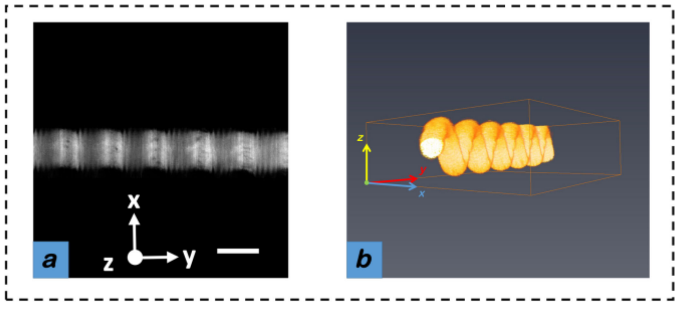

Fig. 5. *En-face* MIP of the full-depth a) and 3-D b) flow imaging of large-tube phantom before synchronizing approach. The scale bar in the figure represents 500 μm.

contributes to the 3-D flow map as given in Fig. 4(g) and Fig. 4(h) which has removed the layers of tubing wall respectively, and demonstrates the advantage and possibility of segmentation. After combining the 3-D flow pictures of all the 21 time points, 4-D imaging can be generated showing varying positions of the flow in a whole cycle of phantom beating. With step motor operating, the position of the flow map kept varying according to the motion path of the phantom thus the function plotted in Fig. 3(a) also worked for the flow map. The 4-D imaging can be obtained in the supplementary material.

The importance of synchronizing approach in reducing the phase mismatching in y-axis can be clarified by the flow imaging before synchronization which is given in both 2-D and 3-D versions as shown in Fig. 5(a) and (b) respectively. Even though the static information was reduced effectively by the OMAG process, the time offset in y-axis locations generated phase mismatching among different cycles. This related to the cyclically spatial distribution of flow map in Fig. 5(b). Actually in a certain OCT system, the high precision of the synchronizing approach always needs the time points during a cycle to be as more as possible [23], [25]. In this paper, 21 time points just resulted in the largest dataset that the system could operate.

Test results of the small-tube phantom using T-OMAG are shown in Fig. 6. Fig. 6(a) is the *En-face* projection of the flow in the small tube and the clear flow map as well as the cross sections of OCT

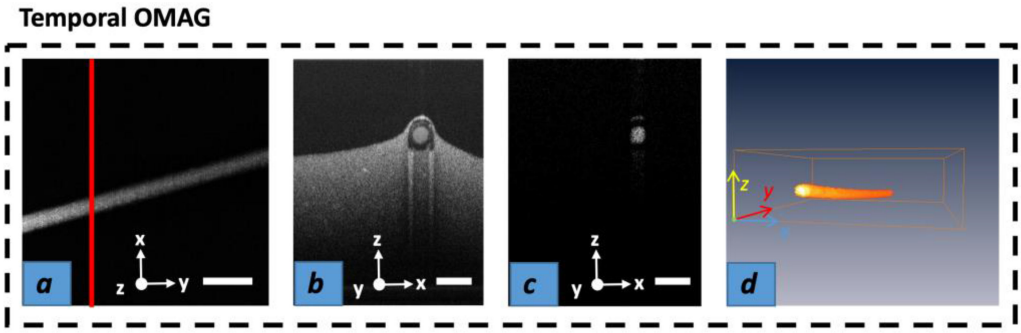

Fig. 6. a) *En-face* MIP of the full-depth T-OMAG flow image acquired in the small-tube phantom. b) Cross section of OCT structure in the red line position in a). c) Cross section of T-OMAG flow in the red line position in a). d) 3-D flow distribution in the small-tube phantom after segmentation. All scale bars in the figure represent 500 μm.

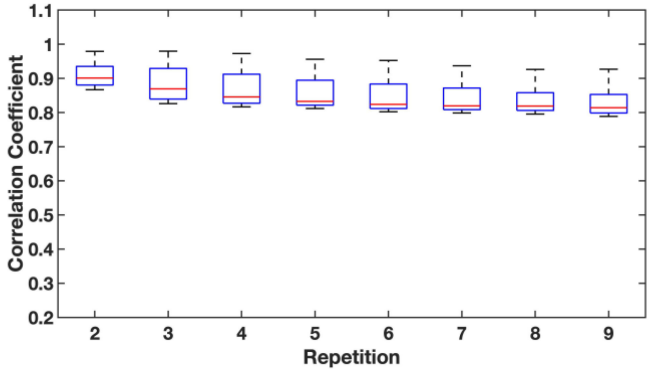

Fig. 7. Correlation coefficients between B-frames with varied repetition in T-OMAG.

structure and flow shown in Fig. 6(b) and Fig. 6(c) respectively. Fig. 6(d) is the 3-D flow map of the small-tube phantom. Compared to the large-tube phantom as the simulation of the coronary vasculature in beating heart, the imaging of the small-tube phantom indicated the flow map of microvasculatures. The 4-D imaging can also be obtained in the supplementary material.

To further qualify the imaging quality using T-OMAG, correlation coefficients between repeated B-frames were calculated for images of all time points by comparing the *N th* frame and the average of other *N-1* frames at the single time point. As shown in Fig. 7, for all 21 time points, even with the increasing repetition in T-OMAG, there would be high correlations $>$80% between B-frames. This would lead to the efficient reduction of static noise by T-OMAG which is given in Fig. 8 showing the signal-to-noise ratio by comparing flow signal and static noise. Obviously, with the increasing of repetition, the signal-to-noise ratio increased, indicating a better reduction in static background applying the more repetition in T-OMAG.

4. Discussion

In this paper, temporal OMAG was developed to image flowing particles in the presence of cyclic motions. Due to the re-distribution of the dataset in temporal domain, T-OMAG processes the signal corresponding to the same motion phase and the flow map of this motion phase can be achieved. This can effectively avoid the decorrelation between B-frames and the artifacts caused by the motion. After combining the flow images at all time points in a whole motion cycle, 4-D imaging of the flow information could be observed, indicating the detail process of motion-causing changes in flow maps at varied positions. To test the feasibility of T-OMAG, a home-made SD-OCT system

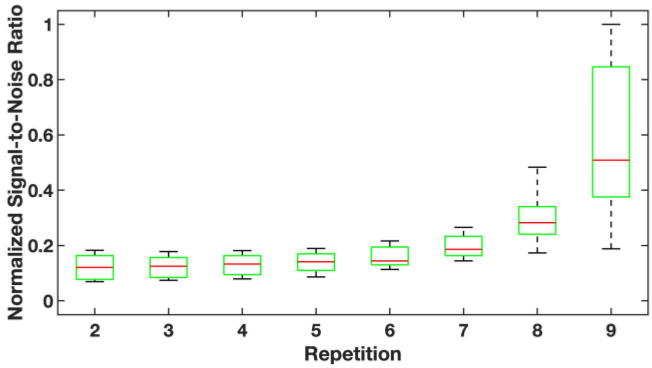

Fig. 8. Normalized signal-to-noise ratio with varied repletion in T-OMAG.

combing a simulating system of cyclic motion was applied in a phantom experiment. With the working of the motion simulator, phantoms could move freely while the moving path was fit to a sine function, similar to the beating of an in vivo heart. After acquiring the dataset as well as processing it, clear flow maps in the large- and small-tube phantoms were observed which failed in the same phantom experiments using classic OMAG. This and the imaging qualification including correlation of B-frames and static signal ratio demonstrated the effectiveness of T-OMAG in imaging moving tissues and obtaining the 4-D imaging in a motion cycle showed T-OMAG as a promising technique in projects related to cyclic moving tissues such as beating heart.

Compared to other approaches and results, T-OMAG with its test results has several advantages. Firstly, T-OMAG could achieve clear flow map in moving phantoms based on a modified OMAG technique while the reports in [28] only showed structure information. This provides researchers with a tool to apply OMAG in scanning cyclically moving tissues. The minimum change in hardware is also an important advantage of T-OMAG. No additional changes and costs are required in the OCT system when applying T-OMAG. Thirdly, as the motion rate was considered in the protocol design, T-OMAG might be more functional in tissues having higher motion rates. In this paper, the motion rate was set to be 6 Hz while the rate in [27] and [28] was 1 Hz and 2 Hz respectively. Obviously, our phantoms were better mimics of real rat heart. In addition to the motion rate, compared to other reports, more time points were recorded in a motion cycle which could generate more 3-D frames in the 4-D video. All these can be helpful in understanding perfusion dynamics of biological tissue in temporal domain while the field of cardiovascular could be a promising application.

However, there are two limitations to the research presented in this paper. Firstly, different than the real vascular imaging where the beating frequency can hardly be constant, the beating rate in the research was precisely known and set. Frankly, the unknown rate will lead to the failure of T-OMAG in imaging beating tissues without external trigger system. In some reports of magnetic resonance imaging, the imaging system was connected to electrocardiogram (ECG) triggering the acquisition of magnetic resonance imaging resulting in the high-quality images of moving tissues [37], [38]. This is also expected to be applied in T-OMAG where ECG would trigger the acquisition of repeated B-frames corresponding to time points in beating cycles. Obviously, this should need the detailed research in both hardware and software which will be done in our future research. Another limitation existed in the protocol design and system. The maximal A-line rate of the camera was 92 kHz while the applied rate was only 67200 Hz in the experiment because of the limitation of dataset in operating system. In our research, the B-frame rate reached 126 fps while the galvo-scanners can reach up to 200 fps. Further optimization in protocol designing as well as system development would enlarge the dataset to be beyond $\sim$57.6 GB of recent size and make it possible to apply the higher-rate galvo-scanners resulting in more time points in each motion cycle.

5. Conclusion

In conclusion, a new numerical method for OMAG processing, temporal OMAG, was developed in imaging a target tissue with repeatable motions. This method can separate the whole motion cycle into several time points and record both OCT structure and flow corresponding to different motion phases. Using a home-made SD-OCT combining with a cyclically beating simulator, large- and small-tube phantom tests were performed and clear images of flow maps in the phantoms were obtained to prove the feasibility of this method. By combining the 3-D distribution of flow at different time points, 4-D imaging was also obtained indicating the possibility of T-OMAG in 4-D research on cyclically moving tissue imaging such as a beating heart.

Acknowledgment

Any opinions, findings, and conclusions or recommendations expressed in this material are those of the author(s) and do not necessarily reflect the views of the funders. The authors also acknowledge Ruikang Wang for his instruction in technology, and Mitchell A. Kirby in manuscript revising.

References

[1] C. M. St. Croix, S. H. Shand, and S. C. Watkins, "Confocal microscopy: Comparisons, applications, and problems," *Bio. Techn.*, vol. 39, no. 6S, pp. 2–5, 2005.
[2] K. K. Shung, "High frequency ultrasonic imaging," *J. Med. Ultrasound*, vol. 17, no. 1, pp. 25–30, 2009.
[3] M. D. Fox and M. E. Raichle, "Spontaneous fluctuations in brain activity observed with functional magnetic resonance imaging," *Nat. Rev. Neurosci.*, vol. 8, no. 9, pp. 700–711, 2007.
[4] D. Huang *et al.*, "Optical coherence tomography," *Science*, vol. 254, no. 5035, pp. 1178–1181, 1991.
[5] P. H. Tomlins and R. Wang, "Theory, developments and applications of optical coherence tomography," *J. Phys. D: Appl. Phys.*, vol. 38, no. 15, pp. 2519–2535, 2005.
[6] W. Drexler and J. G. Fujimoto, "Optical coherence tomography in ophthalmology," *J. Biomed. Opt.*, vol. 12, no. 4, 2007, Art. no. 041201.
[7] M. Machoy, J. Seeliger, L. S. Sommerfeld, R. Koprowski, T. Gedrange, and K. Wozniak, "The use of optical coherence tomography in dental diagnostics: A state-of-the-art review," *J. Healthc. Eng.*, vol. 2017, no. 1, 2017, Art. no. 7560645.
[8] J. Welzel, "Optical coherence tomography in dermatology: A review," *Skin. Res. Technol.*, vol. 7, no. 1, pp. 1–9, 2001.
[9] G. C. Juan Luis *et al.*, "Optical coherence tomography: From research to practice," *Eur. Heart. J. Cardiovasc. Imag.*, vol. 13, no. 5, pp. 370–384, 2012.
[10] T. H. Tsai *et al.*, "Optical coherence tomography in gastroenterology: A review and future outlook," *J. Biomed. Opt.*, vol. 22, no. 12, 2017, Art. no. 121716.
[11] S. Kharchenko, J. Adamowicz, M. Wojtkowski, and T. Drewa, "Optical coherence tomography diagnostics for onco–urology. Review of clinical perspectives," *Cent. Eur. J. Urol.*, vol. 66, no. 2, pp. 136–141, 2013.
[12] S. L. Murphy, J. Xu, and K. D. Kochanek, "Deaths: Final data for 2010," *Nat. Vital Statist. Rep.*, vol. 61, pp. 1–117, 2013.
[13] E. Falk, P. K. Shah, and V. Fuster, "Coronary plaque disruption," *Circulation*, vol. 92, no. 3, pp. 657–671, 1995.
[14] W. Qin, M. A. Roberts, X. Qi, C. E. Murry, Y. Zheng, and R. Wang, "Depth-resolved 3D visualization of coronary microvasculature with optical microangiography," *Phys. Med. Biol.*, vol. 61, no. 21, pp. 7536–7550, 2016.
[15] M. A. Redd *et al.*, "Patterned human microvascular grafts enable rapid vascularization and increase perfusion in infarcted at hearts," *Nature Commun.*, vol. 10, pp. 584, 2019.
[16] S. Huang *et al.*, "In vivo imaging of retinal hemodynamics with OCT angiography and doppler OCT," *Opt. Exp.*, vol. 7, no. 2, pp. 663–676, 2016.
[17] V. J. Srinivasan and H. Radhakrishnan, "Total average blood flow and angiography in the rat retina," *J. Biomed. Opt.*, vol. 18, no. 7, 2013, Art. no. 076025.
[18] L. S. Brea, D. A. D. Jesus, M. F. Shirazi, M. Pircher, T. Walsum, and S. Klein, "Review on retrospective procedures to correct retinal motion artefacts in OCT imaging, " *Appl. Sci.*, vol. 9, no. 13, 2019, Art. no. 2700.
[19] J. L. Tremoleda, K. Alvarez, A. Aden, R. Donnan, A. T. Michael-Titus, and P. H. Tomlins, "Heart-rate sensitive optical coherence angiography for measuring vascular changes due to posttraumatic brain injury in mice," *J. Biomed. Opt.*, vol. 22, no. 12, Art. no. 121710,2017
[20] W. Kang *et al.*, "Motion artifacts associated with in vivo endoscopic OCT images of the esophagus, " *Opt. Exp.*, vol. 19, no. 21, pp. 20722–20735, 2011.
[21] M. Gargesha, M. W. Jenkins, A. M. Rollins, and D. L. Wilson, "Denoising and 4D visualization of OCT images," *Opt. Exp.*, vol. 16, no. 16, pp. 12313–12333, 2008.
[22] A. Mariampillai *et al.*, "Doppler optical cardiogram gated 2D color flow imaging at 1000 fps and 4D in vivo visualization of embryonic heart at 45 fps on a swept source OCT system," *Opt. Exp.*, vol. 15, no. 4, pp. 1627–1638, 2007.
[23] M. Liebling, A. Forouhar, M. Gharib, S. Fraser, and M. Dickinson, "Four-dimensional cardiac imaging in living embryos via postacquisition synchronization of nongated slice sequences," *J. Biomed. Opt.*, vol. 10, no. 5, 2005, Art. no. 054001.

[24] M. Liebling, A. S. Forouhar, M. Gharib, S. E. Fraser, and M. E. Dickinson, "Wavelet-based synchronization of nongated confocal microscopy data for 4–D imaging of the embryonic heart," *Proc. SPIE*, vol. 5914, 2005, Art. no. 591409.
[25] A. L. Lopez III, S. Wang, K. V. Larin, P. A. Overbeek, and I. V. Larina, "Live four-dimensional optical coherence tomography reveals embryonic cardiac phenotype in mouse mutant," *J. Biomed. Opt.*, vol. 20, no. 9, 2015, Art. no. 090501.
[26] A. Liu, R. Wang, K. L. Thornburg, and S. Rugonyi, "Efficient postacquisition synchronization of 4-D nongated cardiac images obtained from optical coherence tomography: Application to 4-D reconstruction of the chick embryonic heart," *J. Biomed. Opt.*, vol. 14, no. 4, 2009, Art. no. 044020.
[27] M. W. Jenkins *et al.*, "4D embryonic cardiography using gated optical coherence tomography," *Opt. Exp.*, vol. 14, no. 2, pp. 736–748, 2006.
[28] O. A. Grishina, S. Wang, and I. V. Larina, "Speckle variance optical coherence tomography of blood flow in the beating mouse embryonic heart," *J. Biophotonics*, vol. 10, no. 5, pp. 735–743, 2017.
[29] R. Wang, "Optical microangiography: A label-free 3-D imaging technology to visualize and quantify blood circulations within tissue beds in vivo," *IEEE J. Sel. Topics Quantum Electron.*, vol. 16, no. 3, pp. 545–554, 2010.
[30] G. Lamouche *et al.*, "Intravascular optical coherence tomography on a beating heart model," *J. Biomed. Opt.*, vol. 15, no. 4, 2010, Art. no. 046024.
[31] H. Sei *et al.*, "Age-related changes in control of blood pressure and heart rate during sleep in the rat," *Sleep*, vol. 25, no. 3, pp. 279–285, 2002.
[32] R. Wang and L. An, "Doppler optical micro-angiography for volumetric imaging of vascular perfusion in vivo," *Opt. Exp.*, vol. 17, no. 11, pp. 8926–8940, 2009.
[33] M. Liebling, A. S. Forouhar, M. Gharib, S. E. Fraser, and,M. E. Dickinson, "Four-dimensional cardiac imaging in living embryos via postacquisition synchronization of nongated slice sequences," *J. Biomed. Opt.*, vol. 10, no. 5, 2005, Art. no. 054001.
[34] X. Yin, J. R. Chao, and R. K. Wang, "User-guided segmentation for volumetric retinal optical coherence tomography images," *J. Biomed. Opt.*, vol. 19, no. 8, 2014, Art. no. 086020.
[35] Q. Zhang *et al.*, "Projection artifact removal improves visualization and quantitation of macular neovascularization imaged by optical coherence tomography angiography," *Ophthalmol. Retina.*, vol. 1, no. 2, pp. 124–136, 2017.
[36] Y. Li, A. Rakymzhan, P. Than, and R. Wang, "Procedure and protocols for optical imaging of cerebral blood flow and hemodynamics in awake mice," *Biomed. Opt. Exp.*, vol. 11, no. 6, pp. 3228–3300, 2020.
[37] J. Oster and G. D. Clifford, "Acquisition of electrocardiogram signals during magnetic resonance imaging," *Physiol. Meas.*, vol. 38, no. 7, pp. R119–R142, 2017.
[38] M. S. Nacif, A. Zavodni, N. Kawel, E. Choi, J. A. C. Lima, and D. A. Bluemke, "Cardiac magnetic resonance imaging and its electrocardiographs (ECG): Tips and tricks," *Int J. Cardiovasc. Imag.*, vol. 28, pp. 1465–1475, 2012.